TAO, Vol. 13, No. 1, 65-90, March 2002

An Infrared Rainfall Algorithm for the MCSs Prevailing over the South China Sea in the Mei-Yu Season

Wann-Jin Chen[1,*] and Ching-Chung Li[1]

(Manuscript received 22 June 2001, in final form 18 February 2002)

ABSTRACT

The goal of this paper is to evaluate the feasibility of the Geostationary Operational Environmental Satellite (GOES) Precipitation Index (GPI) technique for the mesoscale convective systems (MCSs) prevailing over the northern part of the South China Sea in the Mei-Yu season. The rain rate retrievals using the Tropical Rainfall Measuring Mission (TRMM) Microwave Imager were used as the oceanic validation data. The global rain threshold, 235 K, and the global GPI coefficient, 3 mm/h, of the GPI technique were adjusted using a method combining the microwave and infrared rain observations from the TRMM satellite. Once the TRMM rainfall observations were not available, IR rain observations from the Japanese Geostationary Meteorological Satellite 5 (GMS-5) provided rainfall information off shore using the adjusted GPI formula. During a period with numerous rainfalls (from 1 May to 12 June 1998), a total of 60 TRMM overpasses were computed in the statistics. Nineteen of these overpasses contained active convections. The average IR rain threshold is 216 K for cases with a spatial averaging scale of 1°. This technique cannot provide adequate rainfall information under such spatial and temporal requirements for the overpasses without active convections. The optimal advantage of the adjusted GPI technique is the simplicity of its calculation and that it demonstrates adequate ability for monitoring MCS induced rainfalls.

(Key words: Mei-Yu, MCS, The South China Sea, TRMM, GMS-5, GPI)

1. INTRODUCTION

During the Mei-Yu season, the regions around the northern portion of the South China Sea experience numerous disasters such as flash floods and mountainous mudslides caused by heavy rainfall induced by mesoscale convective systems (MCS) from the ocean. Unfortunately,

---

[1] Department of Applied Physics, Chung Cheng Institute of Technology, National Defense University, Ta-Hsi, Tao-Yuan, Taiwan, ROC

[*] *Corresponding author address*: Associate Prof. Wann-Jin Chen, Department of Applied Physics, Chung Cheng Institute of Technology, National Defense University, Ta-Hsi, Tao-Yuan, 335, Taiwan, ROC; E-mail: wannjin@ccit.edu.tw

these oceanic MCS induced heavy rainfalls often cannot be adequately and thoroughly measured due to the lack of sea-based meteorological radar and rain gauges. Satellite infrared (IR) rainfall algorithms can provide overall and frequent rain estimates and aid in the detection of these oceanic MCS induced rainfalls. Most of these algorithms experimentally relate the rainfall amounts to parameters associated with the cloud-top fraction or cloud area (Negri et al. 1984; Arkin and Xie 1994; Goodman et al. 1994; Ebert et al. 1996; Kurino 1997; Vicente et al. 1998; Alder et al. 2001) using techniques such as the Griffith-Woodley technique (Griffith et al. 1978), the auto-estimator (Vicente et al. 1998), the infrared power-law rain rate (IPR) algorithm (Goodman et al. 1994), and the Geostationary Operational Environmental Satellite (GOES) Precipitation Index (GPI) (Arkin 1979; Arkin and Meisner 1987). Their applications concentrate primarily on climate analysis and model initialization. Few of them focus on the instantaneous rainfall observations and real-time flash flood watches (Inoue 1987; Garand 1989; Vicente et al. 1998). The addition of satellite visible (VIS) data efficiently improves the infrared (IR) rain algorithm in reducing high clouds without rains. However, IR radiometers sense radiation emitted from or reflected by the cloud top. Thus, there is no information available on the vertical cloud structure and the near-surface rain layers (Bauer et al. 1998; Hong et al. 1999). Satellite VIS data are only available in the daytime, which limits the improvement space for some algorithms. Passive microwave (MW) radiometers on the other hand physically sense drops and hydrometeors within precipitating clouds, which allows correct multichannel MW measurements of rain regions under the clouds (Ferraro et al. 1994; Wilheit et al. 1991). Although, MW rain retrieval methods use measurements that are more direct than those used for IR rain retrievals, and the instantaneous MW rain estimates are more accurate than IR rain estimates (Ebert et al. 1996), they are, however, limited by the microwave remote sensing technology. Poor temporal scan resolution strategy and narrow scan-swath limit the application of polar-orbiting satellites in both flash flood watches and oceanic heavy rainfall warnings.

Recognizing the shortcomings and advantages in satellite IR and MW rain retrievals, recent studies have used both IR and MW measurements to estimate oceanic rain rates (Kummerow and Giglio 1995; Xu et al. 1999). There have been many IR rainfall algorithms developed by researchers for experimentally monitoring rainfall. For local usage, these algorithms should be validated and evaluated before being applied. Because conventional rainfall observations are very rare over the oceans, the oceanic rain retrievals using the Tropical Rainfall Measuring Mission (TRMM) Microwave Imager (TMI) were set to ground truth for the IR rainfall algorithms. After proper adjustments with microwave rain estimates, the IR rain estimates from geosynchronous satellites with high temporal resolution will be helpful for issuing heavy rainfall warning for short-living MCSs. The goal of this study is to find an already developed IR rainfall algorithm that can provide offshore rainfall information at least on an hourly basis using IR 11-mm data from the Visible and Infrared Spin Scan Radiometer (VISSR) on board the Japanese Geostationary Meteorological Satellite 5 (GMS-5). To avoid the daylight limitation, this IR rainfall algorithm must use IR data only. The satellite VIS data were therefore not used under this consideration. Thus, IR imagery can be mapped into rainfall images directly. An analysis of some IR rainfall algorithm capabilities, limitations, advantages, and weaknesses for rainfall retrieval was made in order to meet the goal of this study.

2. DATA

Four data sets were used in this paper:

- TMI passive microwave measurements obtained during the Mei-Yu season of 1998~2001;
- IR measurements from the VIRS/TRMM and the VISSR/GMS-5 obtained during the Mei-Yu season of 1998~2001;
- Rain accumulation (mm/1-hour) from island rain gauges measured during the Mei-Yu season of 1998~2001; and
- Surface weather classification observed using two buoys deployed during the South China Sea Monsoon Experiment (SCSMEX) held in 1998 (Lau et al. 2000).

The TRMM satellite was launched in November of 1997 (Kummerow et al. 1998), and its inclination to the Equator is 35-degree. The TMI scans the earth with a conical mode, and its antenna beam observes the earth 49 degrees away from nadir, which an incident angle of about 52.8° at the earth's surface. It rotates about the nadir axis at a constant speed of 31.6 rpm, looking forward. Only 130° of the forward sector of every scan is used for getting data. The other sectors are used for calibration and sweep clean data. It takes about 1.9 second for each scan. The TRMM's lower-altitude orbit (350 and 402 km before and after August 2001) results in better spatial resolution and fewer beam-filling problems than the Defense Meteorological Satellite Program (DMSP). The DMSP satellite was launched in 1987 with the first Special Sensor Microwave Imager (SSM/I) aboard (Hollinger et al. 1987). The TMI was improved over the SSM/I with two important changes. The first is a dual-polarized pair of 10.7 GHz channels that increased the dynamic range of rainfall estimates. The other improvement was a slight change in the water vapor channel frequency to 21.3 GHz to reduce saturation in the humid tropics (Simpson et al. 1996). It is a nine-channel passive radiometer with dual (vertical, V, and horizontal, H) polarization channels at 10.7, 19.4, 37 and 85.5 GHz and a vertical polarization channel at 21.3 GHz. In this paper, Tb10V, Tb10H, Tb19V, Tb19H, Tb21V, Tb37V, Tb37H, Tb85V and Tb85H were used to denote the Tbs of channels at 10.7GHz(V), 10.7GHz (H), 19.4GHz (V), 19.4GHz (H), 21.3GHz (V), 37GHz (V), 37GHz (H), 85.5GHz (V) and 85.5GHz (H) respectively. A description of the field of view (FOV) for TMI channels was introduced by Kummerow et al. (1998). The TMI data used in this study are the TMI version-5 Level-1B11 low resolution Tbs. The spatial resolution is about 10 km (Hong et al. 1999). The Level-1B11 data were the instrument data in full resolution with calibration and Earth location computed (Simpson et al. 1996). The TRMM Science Data and Information System (TSDIS) and the TRMM office processed the data. These data are archived and distributed by the Goddard Distributed Archive Center (GDAC). Considering the spatial resolution of the level-1B11 data, the match-up definition of a ground-based measurement and its corresponding TMI Tbs is that the distance measured from the center of the effective field of view to ground-based station is within 5 km and its temporal difference is within 1 hour. The Visible and Infrared Scanner (VIRS) onboard the TRMM satellite is a five-channel radiometer with a visible channel at the 0.63-micron band, a near-infrared channel at the 1.61-micron band, and IR channels at the 3.75-, 11- and 12-micron bands. The VIRS data used in this study are the Level-1B01 data with a spatial resolution of 2.2 km. The Level-1B01 data were the instrument data in full resolution with calibration and Earth location computed (Simpson et al. 1996). The TSDIS and the TRMM office processed the data. These data are archived and distributed by the GDAC.

The GMS-5 satellite was launched in March 1995 into a geostationary obit, 36,000 km in height, located at nominal geodetic coordinates of 0 °N and 140°E. The positioning of the satellite at 140°E gives it an excellent view of the West Pacific regions and the whole of continental Australia. Full disk images are relayed to ground receiving stations approximately 25-28 times per day, providing half-hourly temporal coverage during some periods of the day. The VISSR onboard the GMS-5 satellite can provide IR data with a spatial resolution of 5 km (at nadir) at the 6.7-, 11- and 12-micron bands. Two thermal IR channels are within the atmospheric window (8-14 mm). The 11-µm data were used in this study for retrieving the IR rain intensities. The difference of 11-mm data and 12-µm data was used for cirrus cloud removal. (GMS-5 User's Guide 1997; Prata and Cechet 1999).

Rain accumulation (mm/1-hour) from eight island rain gauges measured during the Mei-Yu season were used as ground truth for satellite rain retrievals. The first island rain gauge is Tarama Jima (24.6°N, 124.7°E) in the Sakishima Gunto (Japan). In addition, there are seven island rain gauges around Taiwan. From north to south, they are Pengchiayu (25.6°N, 122.1°E), Penghu (23.6°N, 119.6°E), Tungchitao (23.3°N, 120.7°E), Lutao (22.7°N, 121.5°E), Liuchiu (22.3°N, 120.4°E), Lanyu (22.0°N, 121.6°E) and Dongsh Island (20.7°N, 116.7°E) (Chen et al. 1999).

In 1998, from May to June, the SCSMEX proceeded in the vicinity of Dongsha Island in the northern portion of the South China Sea. This experiment was designed to study the water and energy cycles in the Asian monsoon regions in order to improve quantitative precipitation predictions. An autonomous temperature line acquisition system (ATLAS) ocean mooring deployed at 20.37 N, 116.52E near Dongsha Island was part of the SCSMEX. It was named the SCS1 buoy in this paper. During the SCSMEX, two acoustic rain gauges (ARGs) were mounted at 20 m and 22 m depths. The mooring deployment lasted from 7 April to 6 June in 1998 (Nystuen et al. 2000). The acoustic data were analyzed by the Applied Physics Laboratory, University of Washington, US to document rainfall and wind conditions at the mooring. The data used in this paper were from the ARG at 20 m. The algorithm classified the weather types using the passive acoustic drifters presented by Nystuen and Selsor (1997). Each recorded spectrum was evaluated to determine the likely geophysical source. The categories were: wind only, rain, drizzle or noise. If "wind only" conditions were detected, the next acoustic sample was 5 minutes later. If "drizzle" was detected, the next sample was 1 minute later and if "rain"was detected the next sample was 30 seconds later. Thus, the time step for the data reported here is not uniform. Another ATLAS rain buoy, which was named the SCS3 buoy, was deployed at 12.98°N, 114.41°E. This buoy provided surface meteorological measurements such as wind velocity and rain accumulation as part of the SCSMEX. The buoy data used in this study were analyzed by the Department of Oceanography, National Taiwan University, Taiwan. The data period used in this study was from 14 April to 30 June; the time step for the wind velocity data was 10 minutes, which is 1 minute for rain accumulation.

3. TMI RAIN RETRIEVALS

3.1 Microwave Rainfall Algorithm

Because water is a polar molecule, over the ocean it has a very large dielectric constant at microwave frequencies. This property results in high reflectivity (low emissivity) by the ocean surface (Wilheit and Chang 1980). Thus, the low emissivity of the sea surface provides a good cold background for viewing particles above the ocean with relatively higher emissivities, such as rain. Therefore, some emission rainfall algorithms rely upon the amount of extra radiation emitted by the precipitation particles against a radiometrically cold ocean surface. Because land surfaces have emissivities in the range 0.8-0.95, these emission rainfall algorithms are not suitable for over-land applications as the high surface emissions effectively mask the precipitation attenuation (Kidd et al. 1998). The scattering rainfall algorithms, on the other hand, rely on the general cooling in the high-frequency channels due to the scattering of ice in the upper portions of many raining clouds (Kummerow and Giglio 1994).

The radiative transfer processes of rain can be separated into two regimes: the attenuation regime and the scattering regime (Wilheit et al. 1991). The microwave Tbs observed in the attenuation regimes represents observations of the liquid hydrometeors within the rain cloud, which may be considered direct measurements of the rainfall. Conversely, the microwave Tbs observed in the scattering regime depends on the many details of the ice layer. Therefore, the satellite microwave Tbs may be divided into attenuation-based measurements and scattering-based measurements. The factors determining the type of attenuation encountered are the size of precipitation particle, the phase of the particle (ice or liquid), and the wavelength of the radiation (Kidd et al. 1998).

Island rain gauge data can be used as ground-truth data coincident with the satellite rainfall observations (Chen and Li 2000). Rainfall observations were treated as the rainfall representatives for the waters around the associated island. The island land effect on the rain retrieval must be evaluated where an island exists within the TMI FOV. Because there is almost no land effect problem for the buoys, their no-rainfall statistics are a good scale for evaluating island land effect. The no-rainfall thresholds are the mean of the no-rainfall statistics from the SCS1 buoy. They were 173.1, 94.1, 216.0, 160.8, 245.0, 275.2 and 258.8 K for the Tb10V, Tb10H, Tb19V, Tb19H, Tb21V, Tb85V and Tb85H respectively. The land effects of eight islands within the study domain (110°E, 15°N ~ 130°E, 30°N) on the passive microwave measurements were examined in this paper. The first island is Tarama Jima in the Sakishima Gunto (Japan). In addition, there are seven island stations around Taiwan. From north to south, they are Pengchiayu, Penghu, Tungchitao, Lutao, Liuchiu, Lanyu and Dongsh Island. According to comparison results (not shown in this paper) of the island no-rainfall statistics and buoy no-rainfall statistics, Tarama Jima, Tungchitao, Pengchiayu, and Dongsha Island were chosen for rainfall characteristic monitoring due to their minor island land effect. The other four islands' TMI no-rainfall measurements deviated from the buoy no-rainfall statistics. The hourly rain measurements from Pengchiayu and Dongsha Island obtained during the Meu-Yu season from 1998 to 2001 were used to establish the linear regression equations with their coincident TMI data. The hourly rain measurements from Tarama Jima and Tungchitao were used as ground-truth data for quantitatively verifying the rain retrievals using the TMI.

Accurate rain identification determines the efficiency of rain retrievals using satellite-based passive microwave radiometers. A rain identification technique's duty is to accurately distinguish the rain signal from environmental noise. The scattering Index (SI) technique using the TMI for identifying oceanic rainfalls was used in this paper. The SI technique originally developed for the SSM/I rain rate estimation technique for recognizing rainy scenes over the oceans (Goodberlet et al. 1989, 1990). By using the multi-channel microwave data from the SSM/I, Grody (1991) used the decision tree method to classify snow cover and precipitation. His study result was improved upon by Ferraro et al. (1994) for presenting the effects of surface conditions on rain identification. After identifying sea ice signals, with the multi-variable linear regression formula as shown in equation (1),

$$SI = -174.4 + 0.72Tb19.4V + 2.439Tb22V - 0.00504Tb22V^2 - Tb85V, \qquad (1)$$

the SI was computed using three vertically polarized SSM/I data over the oceans. In this paper, Tb22V was replaced with Tb21V due to the use of the TMI. For global applications, a value of SI greater than 10 K indicates the presence of both scattering and emission due to rain and generally corresponds to rain rates of 1 mm/h or greater. The SI technique proved adequate performance in the detection of rain areas. Its average identification efficiency for recognizing rainfalls observed by two island rain gauges (Pengchiayu and Dongsha Island) within the Mei-Yu season during a period from 1998 to 2001 is 94.1%. In addition, it is 99.1% for rainfall observations from two buoys (SCS1 and SCS3) deployed in the South China Sea during the SCSMEX. A rainy TMI measurement whose Tb85V and Tb85H are lower than their no-rainfall thresholds was classified as a rain scene associated with scattering-based mechanism due to the scattering characteristics of these channels. Otherwise, it is a rainy event associated with the attenuation-based mechanism.

To define the relationship between the increased Tbs and RRs for emission rainfall algorithms (or decreased Tbs and RRs for scattering rainfall algorithms), one must either utilize theoretically derived relationships between Tbs and RRs or employ regression techniques against ground-truth data (Kummerow et al. 1989; Kummerow and Giglio 1994; Liu et al. 2001). Figure 1 shows the piecewise linear regression algorithm used in this paper for retrieving oceanic RRs. Because, in length, the dynamic ranges of TMI channels are different, in general, it is longer for a TMI channel at lower frequency (Hong et al. 1999). Within the dynamic range, the relationship between RR and TMI Tb is near linear. Within this rainfall algorithm, the entire rainfall range is composed of many piecewise linear regression intervals, and the number of TMI channels within each interval is different. The key point of this rainfall algorithm is to determine which TMI channel can join the multiple-linear regression within a specific piecewise linear regression interval. The relationship between RR and TMI multiple Tbs in this interval is highly linear. This yields a one-to-one function. Figure 2 shows the piecewise linear regression concept. DR_A is the dynamic range for a horizontal polarization TMI channel at 37 GHz. This point A is its saturation point. The emission rainfall algorithm cannot be used for rain retrieval beyond this point due to the saturation problem. The points B and C are saturation points for vertically polarized TMI channels at 21.3 and 10.7 GHz respectively.

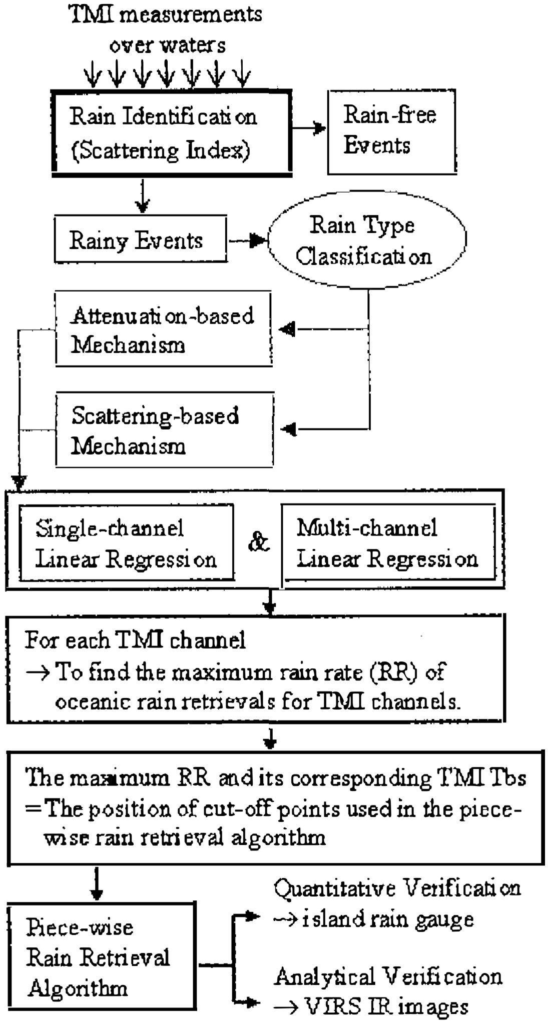

Fig. 1. The description of the piecewise linear rain retrieval algorithm used in this paper.

Within DR_A, all three TMI channels can join the linear regression. To define the three-channel linear regression equation for RR and TMI Tbs, we restricted the domain of this equation to the interval [0, DR_A]. Within DR_B, only TMI channels at 21.3 and 10.7 GHz can join the two-variable linear regression. Again, we restricted the domain for using the two-channel linear regression equation to the interval (DR_A, DR_B]. As above, within DR_C, only the TMI channel at 10.7 GHz can join the single-variable linear regression. We restricted the domain for using the single-channel linear regression equation to the interval (DR_B, DR_C]. Therefore, determining the saturation point is essential for this rain algorithm.

Figure 3 shows the strategy for the piecewise rain retrieval algorithm using the TMI. It is separated into two components in order to deal with rainfalls associated with attenuation-

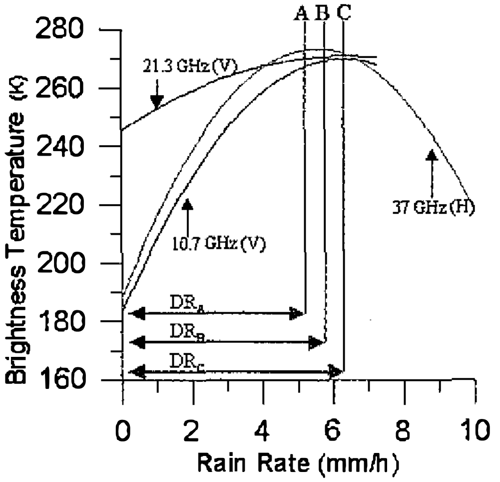

Fig. 2. A concept diagram shows the saturation points and dynamic ranges for TMI channels DR_A is the dynamic range of a horizontal polarization channel with a saturation point A. The relationship between rain rates and Tb37Hs is near linear. The application of the emission rainfall algorithm is restricted in the interval [0 mm/h, DR_A mm/h]. [B and DR_B are for 21.3GHz (V); C and DR_C are for 10.7GHZ(V)].

based or scattering-based mechanism. For attenuation-based mechanism rainfalls, using single-channel linear regression equations for TMI channels, a statistics was carried out in the study domain from 1998 to 2001 in order to obtain the maximum values of the oceanic RRs for each TMI single-channel (Table 1). The maximum RRs for a vertical polarization channel at 10.7 GHz are 16.1, 19.1, 13.5, 18.9 mm/h for the years 1998, 1999, 2000, and 2001 respectively. The minimum value of 13.5 is like the saturation point "C" shown in Fig. 2. The notation of its single-channel linear regression equation is RR1a, and its coefficient of determination (R2) is 0.85 (Garrett and Woodworth 1960). The saturation points used in the rain retrievals for the remaining TMI channels are also shown in Table 1. The definitions for the multiple-channel linear regression equations are shown as in Table 2, with appropriate restrictions on their domains. Table 2 also shows the notations and number of channels involved in the multi-channel linear regression and the available rain retrieval intervals. For example, by definition, the domain for adopting RR17a is the interval (0 mm/h, 3.5 mm/h). The 3.5 is the smallest maximum RR7a value listed in Table 1. Because the dynamic ranges for the channels at 10.7, 19.4, and 21.3 GHz are all longer than this value, seven channels were allowed to join the piecewise rain retrievals within this interval. As long as the RR1a, RR2a, RR3a, RR4a, RR5a, RR6a, RR7a, and RR17a values all fall in this interval, the estimated RR of this TMI point is RR17a (see Fig. 3). Because the TMI channel measurements at 37 GHz might encounter the saturation problem when the rain intensity is heavier than 3.5 mm/h, the RR17a equation is not suitable for retrieving RRs of values beyond 3.5. Under such conditions, the RR15a equation is used to retrieve its rainfall intensity using TMI Tbs at 10.7, 19.4, and 21.3 GHz for those regions with RR values beyond 3.5. Because of the minimum value of the four maximum RR5a values is 4.9 for a TMI channel at 21.3 GHz (see Table 1), by definition, the domain for adopting RR15a is the interval (3.5 mm/h, 4.9 mm/h]. As long as a TMI point's RR1a, RR2a, RR3a, RR4a, RR5a, and RR15a values all fall within this interval, its estimated RR is RR15a (see Fig. 3). As above, the domain of using RR14a was restricted to the interval (4.9 mm/h, 8. 2 mm/h], and only TMI channels at 10.7 and 19.4 GHz jointed the linear regression. In addition, the domain for adopting RR12a was restricted to the intervals (8.2 mm/h, 13.4 mm/h), and

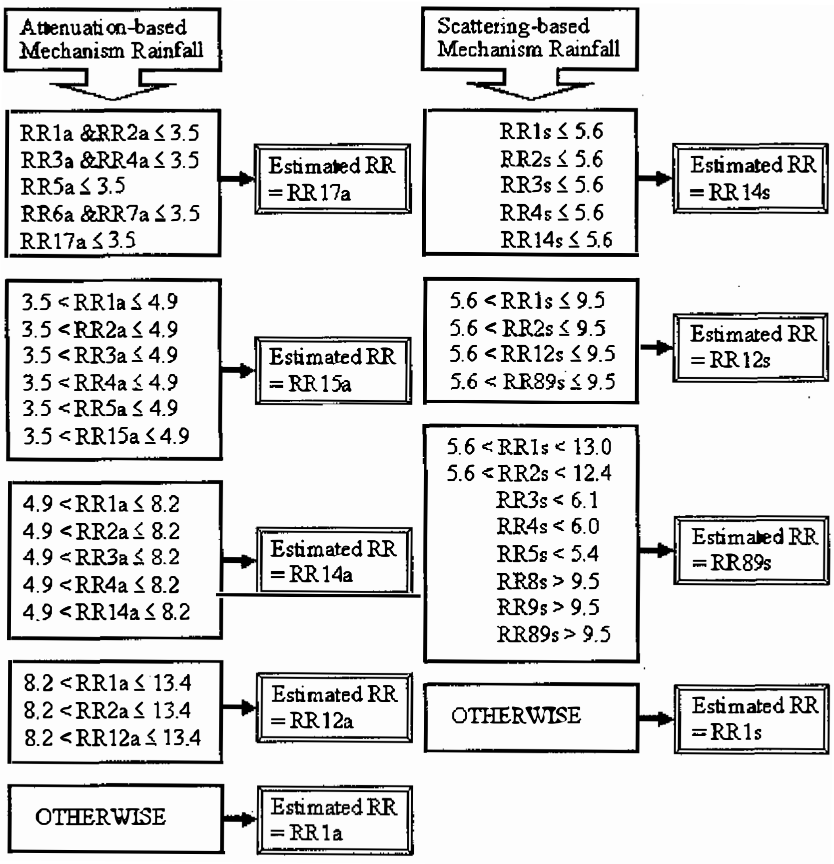

Fig. 3. Strategy of rain retrieval used in each piecewise linear regression interval. Whole rain retrieval range is composed of several piecewise linear regression intervals. It is separated into two components in order to deal with rainfalls associated with attenuation-based or scattering-based mechanism.

only TMI Tbs at 10.7 GHz were used to compute the rain rate values. For a TMI measurement that does not match any one of the restrictions described above, the RR1a is defined as its estimated RR because it has the longest dynamic range of TMI channels (up to 19.1 mm/h retrieved in 1999), and also because the scattering rain algorithm can not be used to study attenuation-based mechanism rainfalls.

Tables 3 and 4 show the single-channel and the multiple-channel linear regression equations for scattering-based mechanism rainfalls, respectively. Their notations, number of channels involved, and available piecewise rain retrieval intervals are also shown in the tables. The scattering-based mechanism rainfall strategy is almost same as the attenuation-based mechanism rainfall method, except for the addition of an approach to study heavy rainfalls using TMI channels at 85.5 GHz (see Tables 3 and 4 and Fig. 3). The third portion of the scattering-based mechanism component shown in Fig. 3 takes advantage of TMI measurements at 10.7,

Table 1. As to attenuation-based mechanism rainfalls, using single-channel linear regression equations for TMI channels, a statistics was carried out in the study domain from 1998 to 2001 in order to obtain the maximum values of oceanic RRs for each TMI single-channel. The maximum RRs for a vertical polarization channel at 10.7 GHz are 16.1, 19.1, 13. 5, 18.9 mm/h for the years 1998, 1999, 2000, and 2001 respectively. The minimum value of 13.5 is like the saturation point "C" shown as in Fig. 2.

Attenuation-based mechanism Single-channel Linear Regression Equations RR (mm/h) ; Tb (K)	Notation	R2	Maximum Retrieved Rain Rate (RR)				
			1998	1999	2000	2001	minimum
RR= 0.272Tb10V−47.018	RR1a	0.85	16.1	19.1	13.5	18.9	13.5
RR= 0.150Tb10H−14.180	RR2a	0.81	15.9	18.9	13.4	18.2	13.4
RR= 0.141Tb19V−30.822	RR3a	0.82	8.7	9.0	8.3	8.5	8.3
RR= 0.078Tb19H−13.142	RR4a	0.80	8.3	8.8	8.2	8.3	8.2
RR= 0.156Tb21V−38.1893	RR5a	0.92	5.3	5.5	4.9	5.3	4.9
RR= 0.066Tb37V−14.6018	RR6a	0.63	4.0	3.9	3.9	3.9	3.9
RR= 0.030Tb37H−4.7360	RR7a	0.58	3.5	3.5	3.5	3.5	3.5

Table 2. The definitions of multiple-channel linear regression equations with appropriate restrictions on their domains for attenuation-based mechanism rainfalls. Their notations, number of channels involved in multiple-channel linear regression, and available rain retrieval intervals are also shown in the table.

Attenuation-based mechanism Multi-channel Linear Regression Equations RR (mm/h) ; Tb (K)	Notation	Number of Channels	Available Rain Retrieval Interval
RR= -32.64−0.50Tb10V+0.84Tb10H−0.97Tb19V +0.19Tb19H+0.81Tb21+0.22Tb37V+0.19Tb37H	RR17a	7	RR ≦ 3.5
RR= -243.24−1.11Tb10V+2.0Tb10H−0.72Tb19V −1.41Tb19H+1.32Tb21	RR15a	5	RR ≦ 4.9
RR= -271.76−0.63Tb10V+0.92Tb10H+2.65Tb19V −1.69Tb19H	RR14a	4	RR ≦ 8.2
RR= -67.92+0.45Tb10V−0.10Tb10H	RR12a	2	RR ≦ 13.4

19.4, 21.3, and 85.5 GHz. It is dedicated to clarify whether the real rain rate interpreted by this TMI measurement beyond the saturation points of channels at 10.7, 19.4, and 21.3 GHz or not. The key point is that, within the emission rain algorithm, for a TMI point, rain rate estimation computed using a single-channel linear regression equation will not be heavier than its maximum value computed from 1998 to 2001. For example, it is 13 mm/h for a vertical polarization channel at 10.7 GHz (see Table 3). Thus, as to a TMI point with a rain rate heavier than 13

Table 3. Same as that shown in table1, but for scattering-based mechanism rainfalls.

Scattering-based mechanism Single-channel Linear Regression Equations RR (mm/h) ; Tb (K)	Notation	R2	Maximum Retrieved Rain Rate (RR)				
			1998	1999	2000	2001	minimum
$RR=0.132Tb10V-22.390$	RR1s	0.79	10.1	11.2	9.7	13.0	9.7
$RR=0.073Tb10H-6.440$	RR2s	0.79	9.6	10.8	9.5	12.4	9.5
$RR=0.095Tb19V-20.687$	RR3s	0.89	5.8	6.1	5.7	6.1	5.7
$RR=0.053Tb19H-8.831$	RR4s	0.89	5.7	5.8	5.6	6.0	5.6
$RR=0.164Tb21V-40.557$	RR5s	0.78	5.2	5.2	5.0	5.4	5.0
$RR=-0.254Tb85V+69.378$	RR8s	0.68	48.9	47.5	47.2	46.8	46.8
$RR=-0.286Tb85H+75.855$	RR9s	0.63	51.7	50.1	48.9	46.9	46.9

Table 4. Same as that shown in table 2, but for scattering-based mechanism rainfalls.

Scattering-based mechanism Multi-channel Linear Regression Equations RR (mm/h) ; Tb (K)	Notation	Number of Channels	Available Rain Retrieval Interval
$RR=-0.13+2.33Tb10V-1.27Tb10H-2.62Tb19V+1.43Tb19H+0.19Tb21$	RR15s	5	$RR \leqq 5.0$
$RR=17.51+1.72Tb10V-0.95Tb10H-1.87Tb19V+1.09Tb19H$	RR14s	4	$RR \leqq 5.6$
$RR=-25.02+0.15Tb10V-0.01Tb10H$	RR12s	2	$RR \leqq 9.5$
$RR=73.65-0.19Tb85V-0.09Tb85H$	RR89s	2	Heavy Rainfalls

mm/h, the equation RR1s will underestimate its intensity due to the saturation problem existed in the emission rain algorithm. In other words, a heavy rain retrieval component using channels at 85.5 GHz must be included in the rain retrieval algorithm. When the computed RR1s, RR2s, RR3s, RR4s, and RR5s are all less than the possible maximum values, and, on the contrary, channels at 85.5 GHz all observed it a heavy rainfall, then the estimated RR of this TMI point is RR89s.

3.2 Verification

The quantitative verification of the piecewise rain retrieval algorithm was carried out using the island rain gauge data from Tungchitao and Tarama Jima as ground-truth data. Statistics were made only for samples with RRs heavier than 1.5 mm/h due to the minor land effects on the passive microwave measurements. The scatter plot of estimated RRs and observed RRs is shown as in Fig. 4, and, using a linear regression technique through origin, the R2 is 0.8. The analytical verification was made using both VIRS IR image and available radar observation. The VIRS IR image was used to see whether the retrieved rain regions matched

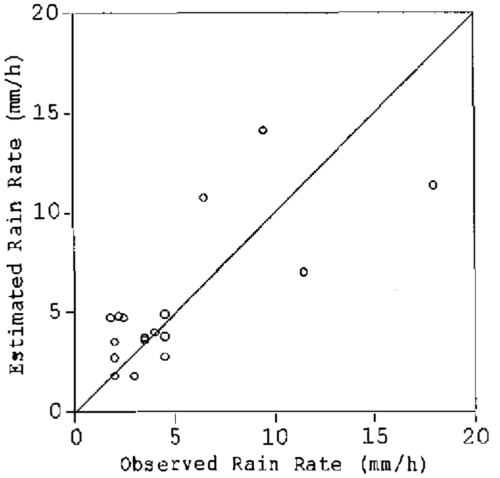

Fig. 4. A scatter plot of TMI RR retrievals and observed RRs shows the quantitative verification of the piecewise rain retrieval algorithm. Hourly island rain gauge data from Tungchitao and Tarama Jima were used as ground-based validation data. Statistics were made only for samples with RRs heavier than 1.5 mm/h, and, using a linear regression technique through origin, the coefficient of determination is 0.8.

possible rain clouds or not. When the retrieved rain regions existed over the clear sky area, the analytical verification fails. In addition, the radar echo intensity is a good parameter for analytically verifying the retrieved rain rates using the TMI. A sample of the TMI RR retrievals for an oceanic MCS occurring in the northern part of the South China Sea at 0018Z 2 June 1998 observed by the TRMM satellite (Fig. 5). Top panel is a VIRS 11μm IR image that shows a MCS occurring to the east of Dongsha Island. The bottom panel shows its corresponding plan position indicator (PPI) plot of the C-POL radar installed at Donsha Island showing four rain regions (A, B, C, D). The maximum reflectivity values for rain regions A, B, C, D observed within ranges of 40~50, 25~30, 30~35, and 35~40 dBZ respectively. Its corresponding TMI RR retrievals are shown in Fig. 6. The background is the VIRS 11-μm IR brightness temperature ($IRTb_{11}$). The numbers denote the rainy TMI points. According to hourly IR images made by the GMS-5 satellite, this cloud system was first observed at 1933Z 1 June growing at the same position. At 2333Z 1 June, the top portion came out and gradually moved northeastward. It merged with a cloud cluster to its west after 0333Z 2 June. After 0033Z 2 June, the coldest cloud top from the bottom portion moved northward dissipated after 0133Z 2 June (top panel of Fig. 7). At 0233Z, the bottom portion began to disappear (bottom panel of Fig. 7). It totally disappeared at 0333Z. The TRMM satellite observed the bottom cloud system during the decaying stage.

Within rain region A, shown in Fig. 6, most of the heavier rainfalls occurred over regions with deep temperature gradient. These rainfall regions were also observed in the forward portion of the MCS. Rain region C existed between two high cloud masses with a deep temperature gradient. Worth noting is that the C-POL radar observed a broad area of low reflectivity and the TMI RR retrievals were all light rainfalls within this region. According to the GMS-5 IR images, at that moment, the coldest cloud top moved northward. As above, this rain occurred over regions with a deep temperature gradient (in the forward portion of the bottom MCS), except that this system was in the decaying stage. In addition, the C-POL radar and the TMI both observed light rains over regions B and C. Worth noting is that both C-POL and TMI observed no rainfall under the coldest cloud top of this decaying cloud system. Results

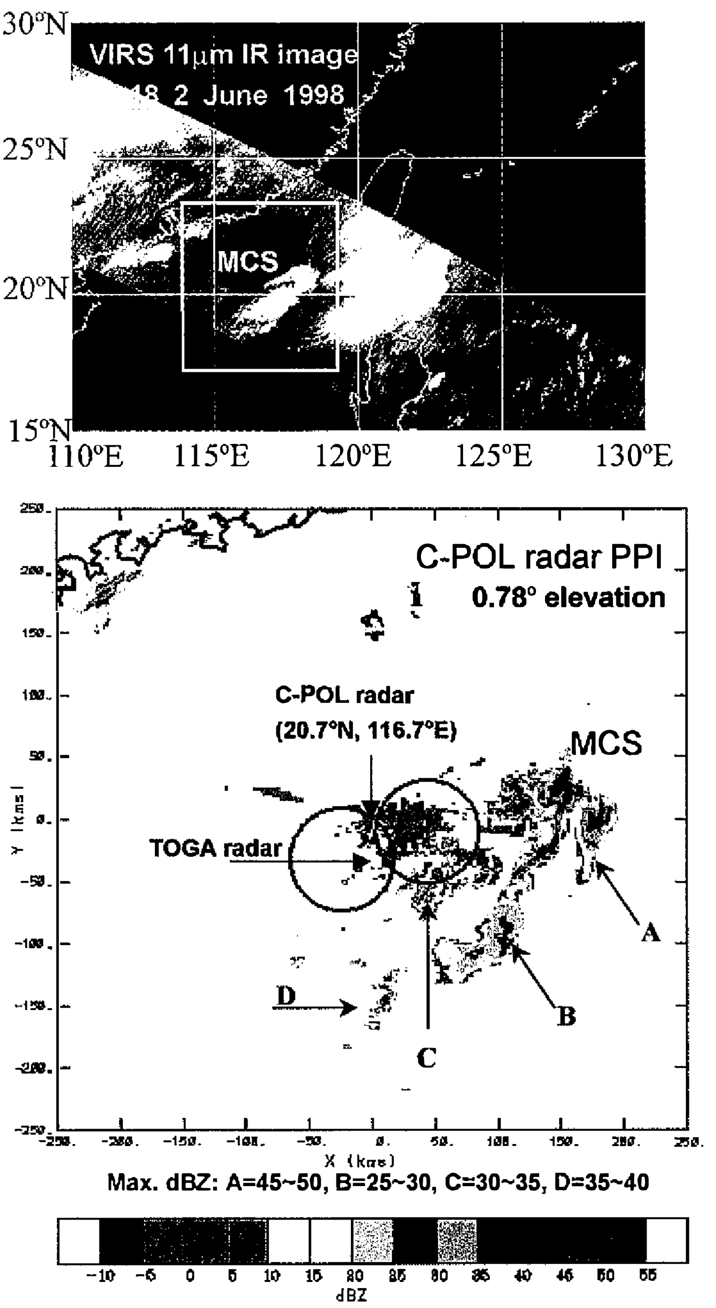

Fig. 5. Top panel is a VIRS 11mm IR image that shows an MCS occurring to the east of Dongsha Island at 0018UTC 2 June 1998. Bottom panel shows its corresponding PPI of the C-POL radar installed at Donsha Island showing four rain regions (A, B, C, D). Its corresponding TMI RR retrievals are shown in Fig. 6. Small circles indicate the dual-Doppler lobes.

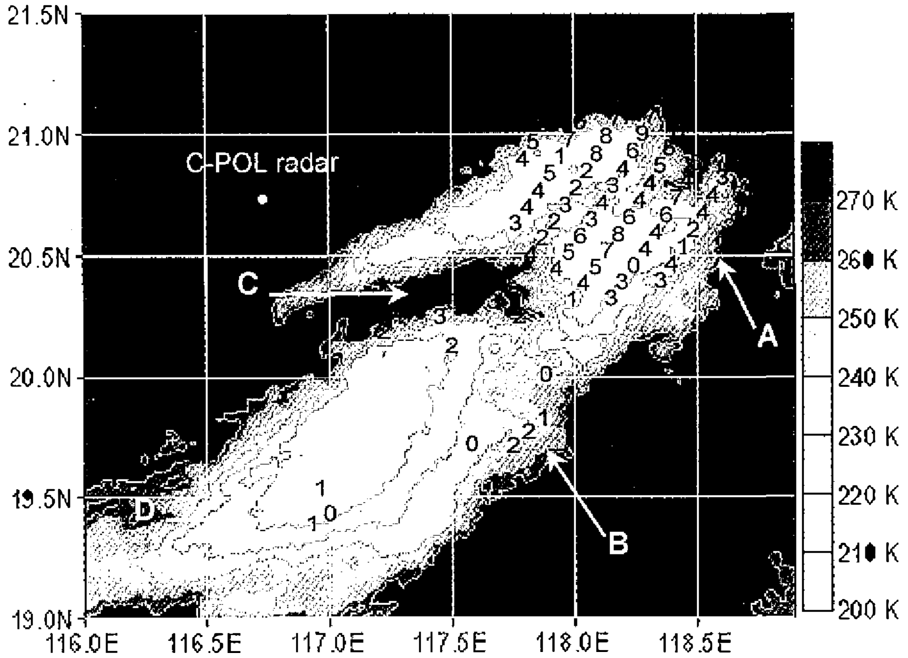

Fig. 6. The numbers printed on the figure denote the TMI RR (mm/h) retrievals for the MSC shown in figure 5, which are shown as their closest whole numbers. The background is the VIRS 11-mm IRTbs (K).

show that the TMI rain retrievals agree with the C-POL radar rainfall observations very well. The TMI rain retrievals and the C-POL radar rainfall observations are reasonable according to the GMS-5 IR images.

4. IR RAIN RETRIEVALS

As mentioned above, the applications of IR rain retrievals concentrate primarily on climate analysis and model initialization. Few of them focus on the instantaneous rainfall observations and real-time flash flood watches. One essential assumption for the IR rainfall algorithms is that colder cloud-tops in the IR imagery can produce greater quantities of rain than warmer cloud-tops. However, the heaviest RRs are not necessarily located under the coldest cloud-tops (see Figs. 5 and 6) and modest RRs or no-rainfall events can be retrieved under the coldest cloud-tops, which is why it is difficult to obtain accurate rainfall information only from the IR data. The life cycle effect and the removal of cirrus clouds are two major obstacles for the IR rain retrievals. As mentioned above, a MCS in the decaying stage was observed by the TRMM (orbit #2935) at 0018Z 2 June, 1998. There was a wide and cold cloud-top with no rain observed under this high cloud. Is it a cirrus cloud with no rain? The removal of thin cirrus with no precipitation is also very important for developing a satellite IR rainfall algorithm. Inoue (1987) presented a cloud classification method using the Advanced Very High Resolu-

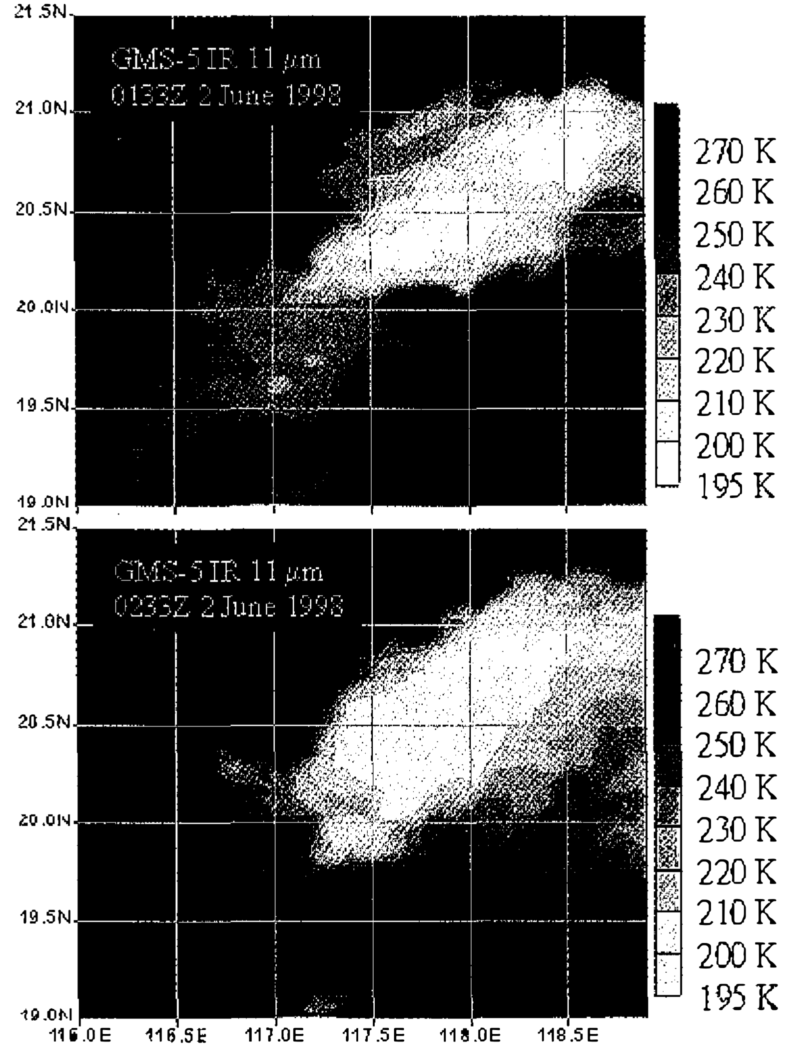

Fig. 7. The cloud system shown in figure 6 was first observed at 1933Z 1 June, and it was growing at same position. After 0033Z 2 June, the coldest cloud top of the bottom portion moved northward, and it was dissipating after 0133Z 2 June (top panel). At 0233Z, the bottom portion almost disappeared (bottom panel), and then it totally disappear at 0333Z.

tion Radiometer (AVHRR) onboard the National Oceanic and Atmospheric Administration 7 (NOAA-7) satellite. It is based on a threshold technique in the two-dimensional histogram whose axes are the IR 11mm brightness temperature ($IRTb_{11}$) and the difference between the $IRTb_{11}$ and the $IRTb_{12}$ ($IRTb_{11-12}$), and cirrus is identified by $IRTb_{11-12}$ in the range greater than 2.5 K. Moreover, in a study on developing a satellite IR technique for estimating "deep/shallow" precipitation using the VISSR/GMS-5, Kurino (1997) also found a relatively low probability of rain occurrence (less than or equal to 30%) appearing in the IRTb$_{11-12}$ range greater than 3 K and IRTb$_{11}$ warmer than or equal to -55°C (218 K). Based on their study results, an IRTb$_{11-12}$ map for the MCS discussed above is shown in Fig. 8 superimposed by two IRTb$_{11}$ isotherms of 218 and 273 K. As shown in Fig. 8, most of the cloud layers were concluded by the 273 K isotherms. Using a screening method introduced by Kurino (1997), clear sky regions were also identified as no-rainfall area (IRTb$_{11}$ > 218 K and IRTb$_{11-12}$ > 2.5 K). A small suspicious region for cirrus (IRTb$_{11-12}$ > 3 K) existed in the middle of the cloud system on the top. The cloud system on the bottom was also not a region covered by thin cirrus (IRTb$_{11}$ < 218 K). This observation shows the life cycle effect is a worthwhile issue for the IR rainfall algorithm. Using the TMI-RRs as ground truth, three IR rainfall algorithms: the Griffith-Woodley technique (Griffith et al. 1978), the auto-estimator (Vicente et al. 1998) or the IPR technique (Goodman et al. 1994), and the GPI technique (Arkin and Meisner 1987) were reviewed and analyzed to find an IR rainfall algorithm capable of operating on one-hourly IR images at resolution of one geometric degree.

4.1 The Power-law Rain Estimation Technique

The power-law rain estimation technique relates surface RRs to cloud-top IRTbs using a

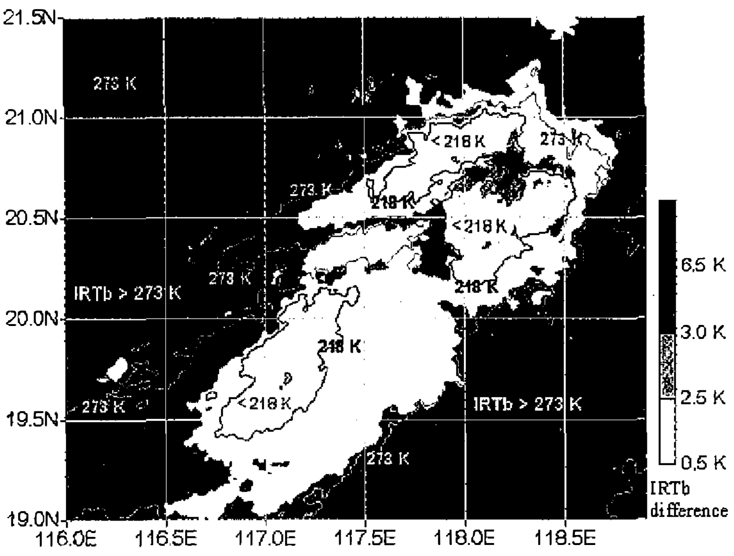

Fig. 8. An IRTb$_{11-12}$ map for the MCS shown in figure 6 is superimposed by two IRTb$_{11}$ isotherms of 218 and 273 K. Most of the cloud layers were concluded by the 273 K isotherms. By using a screening method introduced by Kurino (1997), clear sky regions were also identified as no-rainfall area (IRTb$_{11}$ > 218 K and IRTb$_{11-12}$ > 2.5 K). A small suspicious region for cirrus existed in the middle of the cloud system on the top (IRTb$_{11-12}$ > 3 K), and the cold cloud-tops on the bottom (IRTb$_{11}$ < 218 K) is not a region covered by thin cirrus.

power-law curve fitted formulation. This power-law regression method is a pixel-by-pixel computation technique with high spatial resolution. The heaviest RRs must match the coldest IRTb within this IR rain estimation technique. It was first developed in a radar study of summer storms occurring over south Florida (Gagin et al. 1985). Using the surface rain gauge data as ground truth, the IPR technique performed a correlation coefficient of 0.54 over Amazonia for the period 5~9 May, 1987. The IRTb$_{11}$ data coincide with the gauge locations and the rain accumulation for a period of three hours. In comparison with other IR rainfall algorithms in estimating three-hourly RRs over Amazonia using IR data form the VISSR/GOES, the IR power-law rain estimation (IPR) technique performed as well as the other IR rain estimation techniques (Goodman et al. 1994). According to the scatter plot shown in Goodman et al. (1994), they used the 253.2 K threshold to exclude "dry" anvil cirrus clouds and included "wet" shallow cumulus clouds. The power-law relationship between the observed RRs and IRTbs cannot be established without a point of (23 mm/3h, 195 K). Some low RRs (< 5 mm/3h) were observed under cold clouds (< 210 K), and, on the contrary, some high RRs (> 20 mm/3h) were observed under cloud-tops with IRTbs warmer than 225 K. Along the fitted power-law curve, a RR of 21.6 mm/3h occurs at IRTb$_{11}$ of 190 K, IRTbs for some observed RRs higher than 20 mm/3h fall in a range from 210 to 230 K. A scatter plot of the corresponding TMI-RR/IRTb$_{11}$ points gathered from six well-delineated MCSs observed during the SCSMEX also present a weak power-law pattern (Fig. 9). As in the results from Goodman

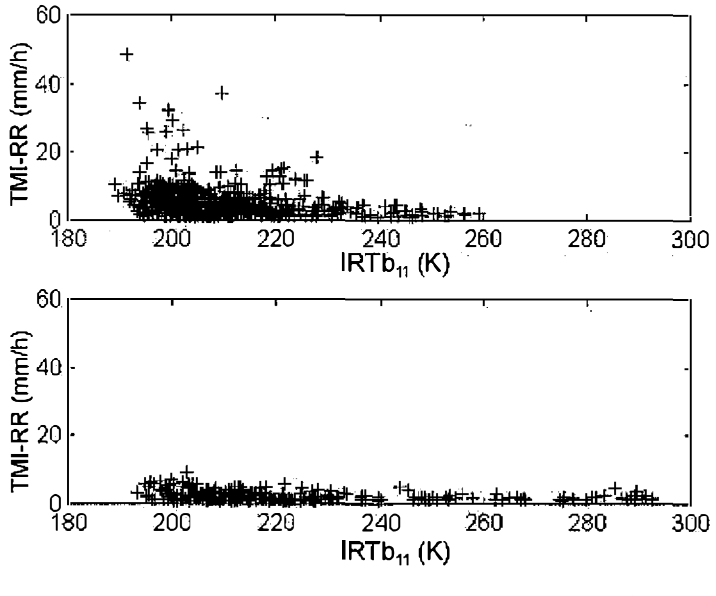

Fig. 9. The scatter plots for corresponding IRTb$_{11}$/ TMI-RR, which show a weak power-law relationship. Abscissa is the retrieved TMI-RRs, and the ordinate is the IRTb$_{11}$. The top panel shows scattering-based mechanism rainfalls occurring at IRTbs lower than 260 K. The attenuation-based mechanism rainfalls occurred in a range from IRTbs lower than 195 K to even 295 K (bottom panel).

et al. (1994), the coldest IRTb cannot match the heaviest TMI-RR, and the cloud-tops over some regions with low RRs are colder than some clouds having heavy rainfalls.

The auto-estimator was an operational GOES IR rainfall estimation technique in the National Environmental Satellite, Data, and Information Service (NESDIS) at NOAA that runs in real time for flash flood forecasting, numerical modeling, and operational hydrology (Vicente et al. 1998). Based on the IPR technique, it was adjusted for different moisture regimes using model generated recent precipitable water and relative humidity fields. Additionally, a mask was computed to restrict the rain to regions using the growth rate and cloud-top temperature gradient correction factors. The main purpose of the moisture, cloud growth rate and cloud-top temperature gradient correction factors was to solve problems caused by cirrus clouds and the life cycle effects. Therefore, with the assistance from cloud models, a proper power-law relationship between observed RRs and IRTbs might be achieved. Otherwise, the power-law relationship between them might be weakly correlated. Vicente et al. (1998) validated the hourly RRs of the auto-estimator using gauge-adjusted radar precipitation products in three distinct cases held in the US. The results showed it had modest skill at one-hour time resolution for a spatial resolution of 12 km. Results improved with larger grid sizes (48×48 km ~ 300×300 km). Thus, the auto-estimator is not an algorithm using satellite IR data only. Without assistance from cloud models or sounding data, the respected performance won't be achieved, especially for the oceanic regions.

4.2 Griffith-Woodley Technique

An accurate estimate of rain areas or rain pixel numbers is very important for the Griffith-Woodley (GW) technique, which is a cloud-by-cloud computation algorithm that linearly relates the cloud area to the rainfall volume. A recent development is to use both IR and VIS data to accurately describe the cloud patches (Xu et al. 1999). However, the VIS data are only available during the day, rendering it unsuitable for developing a technique applicable at night. Significant improvements have been made to the GW technique, such as incorporating life cycle effects, cloud features, and etc. into the method. However, for the Asia-Pacific region, the life cycle effect cannot be added to the GW technique, as it must be computed from at least two IR images within one hour. Therefore, the temporal resolution of the GMS-5 IR data limits the GW technique in determining the cloud life cycle effects on an hourly basis. This in turn significantly affects the retrieval results of the GW technique.

On the other hand, the first step in the GW technique is to obtain the cloud area-rainfall relationship, which can be determined by superimposing the IR imagery onto the surface-radar rain measurements (Griffith et al. 1978) or onto the surface-rain regions identified by the passive microwave measurements (Xu et al. 1999). Over two regions in South Florida, Griffith et al. (1978) found that 80 digital counts and 253 K were useful thresholds to define the cloud area for the VIS and IR data. While using the rain regions identified by the SI technique as ground truth to determine the appropriate IR threshold for a given area, Xu et al. (1999) found that the optimal IR threshold for June was 236 K with an increase to 241 K for July and August over the Japanese islands and adjacent oceanic areas in 1989. Therefore, for local usage, the key to the GW technique is to find the optimal IR rain threshold defining rain clouds. According to a personal communication with Dr. Tai-Kuang Chiou (2000) of the Central Weather Bureau in Taiwan, the operational results from the GW technique are not satisfactory for the detection of heavy rainfall due to the imprecise selection of IR rain threshold. Because conventional rain observations (sea-based gauge and radar) are scarce over the ocean, IR rainfall algorithms need MW rain estimates to provide information on rain-cloud size and the corresponding IR pixel numbers. As long as the minimum detectable MW RR is determined, the size of the rain regions under the cold cloud-tops can be obtained. This in turn would point out the cloud-path, which is colder than a typical IR cloud-top temperature. Within data grids, the MW rain area must be equal to the cloud-patch area. The IR rain threshold is equal to this typical IR cloud-top temperature. In short, the choice of the minimum detectable MW RR seems a key factor in the successful application of this kind of MW and IR combination technique. However, determination of this minimum detectable RR is very subjective and difficult to ascertain. Some significant improvements made to the GW technique using the satellite VIS data changed it into an efficient rainfall algorithm for the daytime only. Thus, like the auto-estimator, it is not an algorithm using satellite IR data only. Without assistance of rain observations and cloud classification from satellite VIS data, the respected performance won't be achieved, especially for the oceanic regions.

4.3 GPI

The GPI technique was first presented by Arkin (1979) and accepted by researchers for monthly rainfall analysis and rainfall climatology studies (Richards and Arkin 1981; Arkin and Meisner 1987; Kummerow and Giglio 1995; Joyce and Arkin 1997). The GPI technique does not deal with pixel-by-pixel computations, but rather seeks the best linear correlation between the cloud-top fractional coverage (Fc), which is colder than certain IRTbs such as 235 K, surface rain accumulations within an area, and during selected time intervals. The linear correlation is stronger during periods and/or for areas of significant rainfall. For light rains the correlation may be too weak to be satisfactory (Richards and Arkin 1981). As long as an adequate average area and time interval are chosen, the location of the heaviest RR is not a decisive factor for the GPI technique. The problems associated with excessive rain areas due to the selection of the minimum detectable RR within other IR rain estimation algorithms are mitigated after taking temporal and spatial averages. For global usage, the common GPI equation is GPI (mm) = 3 (mm/h) × Fc × average period (hours). This formula is obtained from an empirical relationship between the area-averaged rain accumulation and the Fc for cold cloud-tops. The cloud-top Fc was defined as the ratio of the sum of the IR points colder than the IR rain threshold to the point number within a typical region and a period of time (e.g., $1^\circ \times 1^\circ$ grid size and one hour).

During three phases of the Global Atmospheric Research Program (GARP) Atlantic Tropical Experiment, the linear relationship mentioned above was found to be the strongest when 235 K was used as the IR rain threshold. This region must be no less than a $1^\circ \times 1^\circ$ square and is best for a $2.5^\circ \times 2.5^\circ$ box. The temporal averaging scale is from one hour to 24 hours. The original GPI equation should be examined and adjusted according to local weather conditions. For local usage, the first problem in applying the GPI technique is determining the IR rain threshold to estimate the cold cloud fraction. The second is to adjust the GPI coefficient (slope).

In this paper, GPI computations were made with spatial and temporal averaging scales of 1° and one hour respectively. The strategy for combining IR and MW rainfall observations is shown as in Fig. 10. The global rain threshold, 235 K, and the global GPI coefficient, 3 mm/h, were adjusted using a method combining the TMI rain retrievals and IR rain measurements from the VIRS/TRMM. Once the TRMM rainfall observations were not available, the VISSR/ GMS-5 will provide at least one-hourly rainfall information off shore using the TMI-RR adjusted GPI formula.

The IR rain threshold was determined by locating the best linear correlation between the averaged TMI-RRs and Fc for a given VIRS IRTb$_{11}$ over water. Using the TMI RR retrievals as ground truth, the adjusted GPI equations and the best IR rain threshold can be obtained by applying linear regression to the corresponding TMI-RR/ Fc pairs. Here the averaged unconditional RR for each 1°× 1° box was determined by dividing the sum of the TMI-RRs by the TMI point amount regarding rainy and no-rainfall points. Within the study domain, over the ocean, for each 1°× 1° square within a VIRS IR image, 61 Fc values were computed for 61 different cloud-top temperatures ranging from 200 to 260 K with a 1 K increment. Among the 61 TMI-RR/Fc pairs, the best IR rain threshold was the IRTb$_{11}$ of a pair with the highest R2 value. The corresponding TMI-RR/ Fc regression equation, which was called the TMI-RR adjusted GPI equation was then used to estimate hourly rain maps of GPI for successive GMS-5 IR images. Otherwise, for cases that cannot achieve satisfactory R2 values, the global GPI formula with a fixed threshold of 235 K is used to compute GPI rain maps. In order to know the chance of successfully using the method combining the MW and IR rainfall observations introduced above, an exercise was made for 60 TRMM overpasses crossing the waters near Taiwan from 1 May to 13 June 1998. After 13 June, few rainfalls were observed by island rain gauges. Results demonstrated adequate performance ($R2 \geq 0.5$) on 19 of them with an average rain threshold of 216 K, which is lower than the global rain threshold of 235 K. The other 41 VIRS images are cases that include few or have no convections. The chance of successfully using this method was 31% (19/60). Therefore, the TMI-RR adjusted GPI technique with variable rain thresholds demonstrate its feasibility to estimate one-hourly/area-averaged rainfall intensity for each 1°× 1° region during periods with active convections. For overpasses without active convections, this technique cannot provide adequate rainfall information under such spatial and temporal requirements. The chance of successfully using the adjusted GPI technique with a fixed rain threshold of 235 K is 13% (8/60).

Although the spatial resolution for the GPI technique is not enough for analyzing oceanic MCSs and initializing numerical models, the GPI provides direct and reasonable threat information for heavy rainfall warnings and flash flood watches. The adjusted GPI equation proved the feasibility to provide quantitative hourly rain indices of each 1°× 1° square for monitoring MCS heavy rains. Because the speed of computation is another key to the success of real-time heavy rain detection, the optimal advantage of this IR data only technique is the simplicity of its calculation. If the summation of GPIs for an MCS increases with time, the MCS should then be followed for possible heavy rains. For example, by using the MW/IR rain estimation technique shown as in Fig. 10, a case study was used to demonstrate its ability to monitor MCSs. The TRMM overpass #3102 was scanned across Dongsha Island at 2129Z on

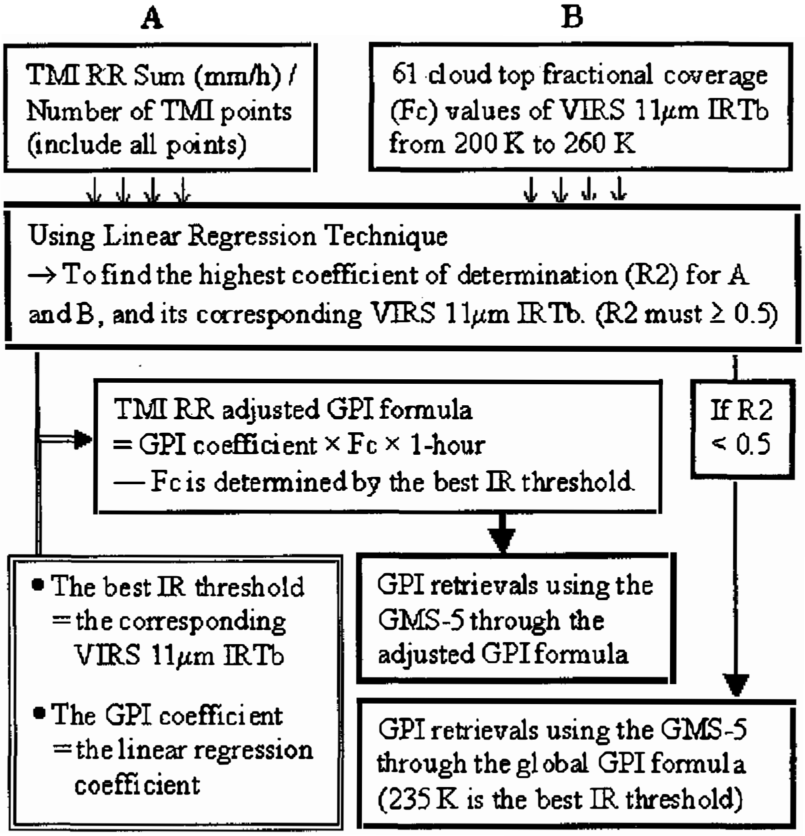

Fig. 10. Within the study domain, over the ocean, for each 1°·1° square within a VIRS IR image, 61 Fc values are computed for 61different cloud-top temperatures ranged from 200 to 260 K with a 1 K increment. Among the 61 TMI-RR/Fc pairs, the best IR rain threshold is the $IRTb_{11}$ of a pair with the highest R2 value. Thus, the global rain threshold, 235 K, and the global GPI coefficient, 3 mm/h, was adjusted using this method, and the TMI-RR adjusted GPI equation was used to estimate rain maps of GPI for successive GMS-5 IR images.

6 June 1998. The next available TRMM overpass was #3023 at 1348Z on 7 June 1998. The TMI-RR adjusted GPI formula for the overpass #3102 was GPI (mm)= 0.21+3.72(mm/h) ×Fc× 1-hour. The IR rain threshold used within the GPI computation was VIRS $IRTb_{11}$ of 221 K, and the R2 value was equal to 0.63. This TMI-RR adjusted GPI equation would be used to retrieve GPI rain maps for successive GMS-5 11mm IR images after 2129Z. Figure 11 shows that there were active convections occurring over the South China Sea from 0133Z to 1233Z on 7 June 1998. Because southwesterly winds prevailed at the time and the GPI summation was increasing with time, these MCSs might bring heavy rains to Taiwan (see Fig. 12). The corresponding GPI rain maps demonstrates the variation of rainfall intensity near Taiwan,

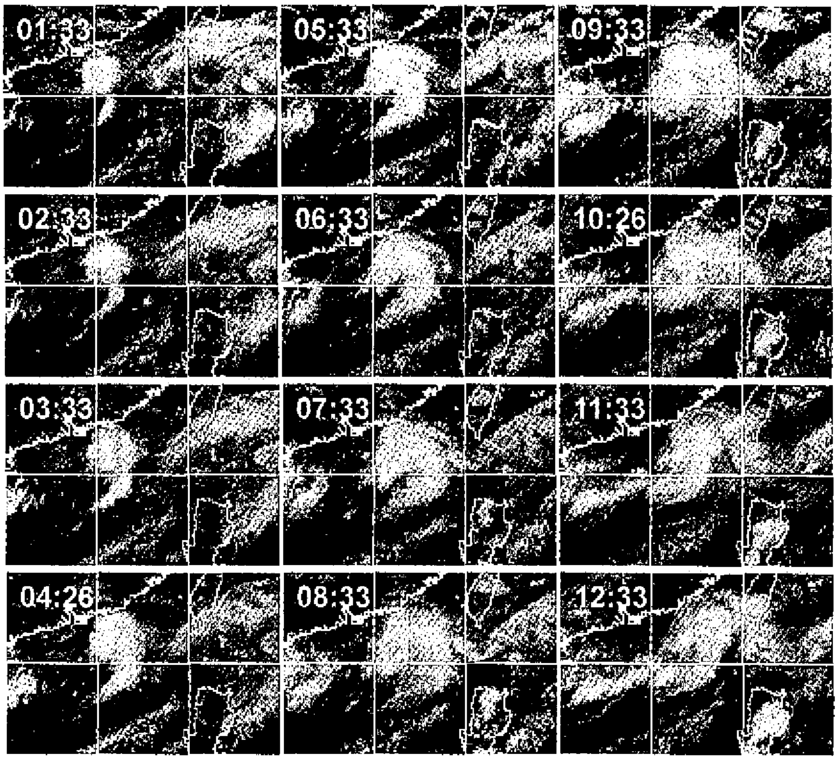

Fig. 11. GMS-5 11 micron IR image series (from 0133Z to 1233Z 7 June) which showed many MCSs prevailed over the northern part of the South China Sea. The position of the upper-left corner is 110°E, 25°N and that for the lower-right is 125°E, 15°N.

and heavy rainfalls occurring over Southern Taiwan at 1233Z on 7 June were also retrieved. Therefore, this is a feasible IR rainfall algorithm for MCSs prevailing in the Mei-Yu season.

5. CONCLUSIONS

Unlike the Griffith-Woodley technique and the IPR technique (or the auto-estimator), the TMI-RR adjusted GPI technique does not need other assistant parameters within rain retrievals. This is a rainfall algorithm that uses satellite IR data only, and therefore it can monitor the Western Pacific regions at a half or one hour frequency using the VISSR/GMS-5. In this paper, the goal was to adjust the global rain threshold, 235 K, and the global GPI coefficient, 3 mm/h, of the GPI technique using a method combining the TMI rain retrievals and IR rain measurements from the VIRS/TRMM. Once the TRMM rainfall observations were not available, the VISSR/GMS-5 will provide rainfall information off shore using the TMI-RR adjusted GPI formula. During a period with numerous rainfalls observed by surface gauges (from 1 May to 12 June 1998), the chance of successfully using the method (R2 ≥ 0.5) combin-

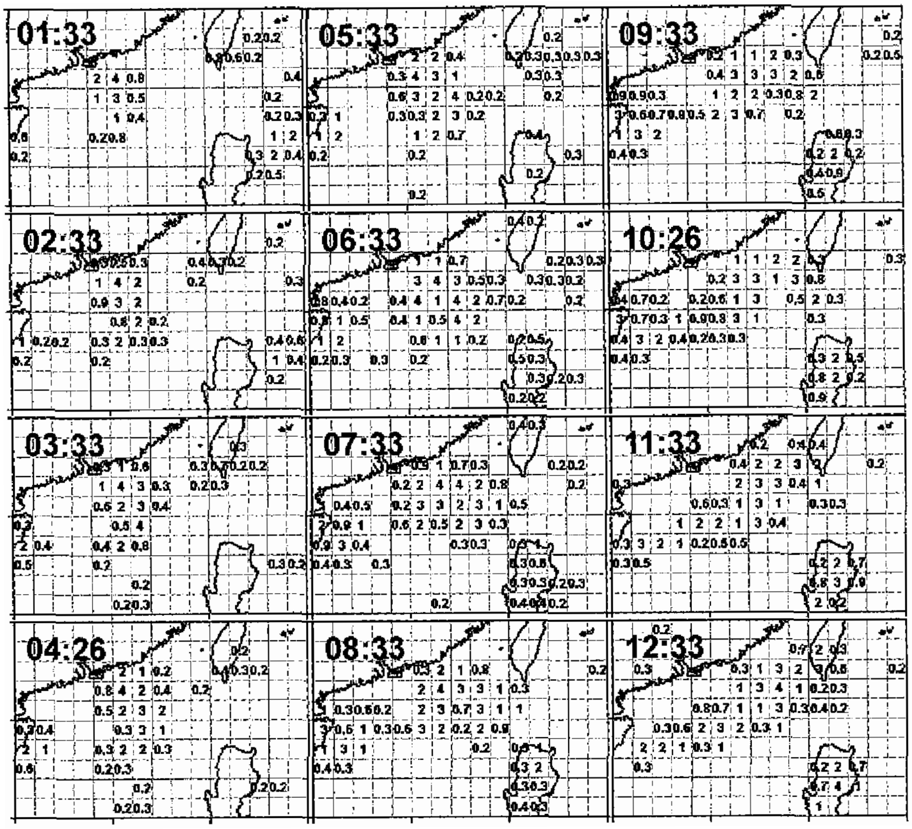

Fig. 12. The GPI rain maps for GMS-5 11 micron IR images. The range of study area is from 110°E, 25°N to 125°E, 15°N, and the interval of grid point is 1°.

ing MW and IR rainfall observations is 31% (19/60). A total of 60 TRMM overpasses were computed in the statistics. Nineteen of these overpasses contained active convections. For a temporal resolution of one hour, the spatial resolution can reach up to 100 km approximately. The average IR rain threshold is 216 K for active convections occurred during the SCSMEX. For overpasses without active convections, this technique cannot provide adequate rainfall information under such spatial and temporal requirements. The chance of successfully using the GPI technique with a fixed rain threshold of 235 K is 13% (8/60). Therefore, the TMI-RR adjusted GPI technique with variable rain thresholds demonstrate its feasibility to estimate one-hourly/area-averaged rainfall intensity for each 1° × 1° region during periods with active convections. Although the spatial resolution for this technique might be not enough for analyzing oceanic MCSs and initializing numerical models, it still provides direct and reasonable threat information for heavy rainfall warnings and flash flood watches. Because the speed of computation is another key to the success of real-time heavy rain detection, the optimal advantage of this IR data only technique is the simplicity of its calculation.

Acknowledgements This study was supported by the TRMM Office at NASA GSFC. We would like to thank Drs. C. Kummerow, L. S. Chiu, A. T. C. Chang and E. J. Nelkin for their help with the TRMM data. Special thanks go to Dr. Tom Keenan, Bureau of Meteorology, Australia for providing the C-POL radar images. We would particularly like to thank the Central Weather Bureau in Taiwan for providing surface rain and GMS-5 data during the period of the SCSMEX.

REFERENCES

Arkin, P. A., 1979: The relationship between fractional coverage of high cloud and rainfall accumulations during GATE over the B-array. *Mon. Wea. Rev.*, **107**, 1382-1387.

Arkin, P. A., and B. Meisner, 1987: The relationship between large-scale convective rainfall and cold cloud over the Western Hemisphere during 1982 - 1984. *Mon. Wea. Rev.*, **115**, 51-74.

Arkin, P. A., and P. Xie, 1994: The global precipitation climatology project: first algorithm intercomparison project. *Bull. Amer. Meteor. Soc.*, **75**, 401-419.

Alder, R. F., C. Kidd, G. Petty, M. Morissey, and H. M. Goodman, 2001: Intercomparison of global precipitation products: The third precipitation intercomparison project (PIP-3). *Bull. Amer. Meteor. Soc.*, **82**, 1377-1396.

Chen, T. C., M. C. Yen, J. C. Hsieh, and R. W. Arritt, 1999: Diurnal and seasonal variations of the rainfall measured by the automatic rainfall and meteorological telemetry system in Taiwan. *Bull. Amer. Meteor. Soc.*, **80**, 2299-2312.

Chen, W. J., and C. C. Li, 2000: Oceanic rain rate retrievals using TRMM Microwave Imager multi-channel brightness temperatures during the 1998 SCSMEX. *TAO*, **11**, 765-788.

Chiou, T. K., 2000: personal communication. Meteorological Satellite Center, Central Weather Bureau in Taiwan.

Ebert, E. E., M. J. Manton, P. A. Arkin, R. J. Allam, G. E. Holpin, and A. Gruber, 1996: Results from the GPCP algorithm intercomparison programme. *Bull. Amer. Meteor. Soc.*, **77**, 2875-2887.

Ferraro, R. R., N. Grody, and G. F. Marks, 1994: Effects of surface conditions on rain identification using the DMSP-SSM/I. *Remote Sens. Rev.*, **11**, 195-209.

Garand, L., 1989: Two automated methods to derive probability of precipitation fields over oceanic areas from satellite imagery. *J. Appl. Meteor.*, **28**, 913-924.

Garrett, H. E. and R. S. Woodworth, 1960: Statistics in phychology and education, Longmans, Green and Co., 478pp.

GMS-5 User's Guide, 1997, Meteorological Satellite Center of Japan, Nakakiyoto, Kyose, Tokyo, 190 pp.

Goodberlet, M. A., C. T. Swift, and J. C. Wilkerson, 1989: Remote sensing of ocean surface winds with the Special Sensor Microwave/ Imager. *J. Geophys. Res.*, **94**, C10, 14547-14555.

Goodberlet, M. A., C. T. Swift, and J. C. Wilkerson, 1990: Ocean surface wind speed measurements of the Special Sensor Microwave/ Imager (SSM/I). *IEEE Trans. Geosci.*

Remote Sens., **28**, 823-827.

Goodman, B., D. W. Martin, W. P. Menzel, and E. C. Cutrim, 1994: A non-linear algorithm for estimating three-hourly rain rates over Amazonia from GOES/VISSR observations. *Remote Sens. Rev.*, **10**, 169-177.

Griffith, C. G., W. L. Woodley, P. G. Grube, D. W. Martin, J. Stout, and D. N. Sikdar, 1978: Rain estimation from geosynchronous satellite imagery- visible and infrared studies. *Mon. Wea. Rev.*, **106**, 1153-1171.

Grody, N. C., 1991: Classification of snow cover and precipitation using the Special Sensor Microwave Imager. *J. Geophys. Res.*, **96**, 7423-7435.

Holinger J., R. Lo, G. Poe, R. Savage, and J. Pierce, 1987: Special Sensor Microwave/ Imager user's guide, NRL Tech. Rep., Naval Research Laboratory, 120 PP.

Hong, Y., C. D. Kummerow, and W. S. Olson, 1999: Separation of convective and stratiform precipitation using microwave brightness temperature. *J. Appl. Meteor.*, **38**, 1195-1213.

Inoue, T., 1987: A cloud type classification with NOAA-7 split-window measurements. *J. Geophys. Res.*, **92**, 3991-4000.

Kidd, C., D. Kniveton, and E. C. Barrett, 1998: The advantages and disadvantages of statistically derived-empirically calibrated passive microwave algorithms for rainfall estimation. *J. Atmos. Sci.*, **55**, 1576-1582.

Joyce, R., and P. A. Arkin, 1997, Improved estimates of tropical and subtropical precipitation using the GOES Precipitation Index. *J. Atmos. Oceanic. Technol.*, **14**, 997-1011.

Kummerow, C., R. A. Mack, and I. M. Hakkarinen, 1989: A self-consistency approach to improve microwave rainfall rate estimation from space. *J. Appl. Meteor.*, **28**, 869-884.

Kummerow, C., and L. Giglio, 1994: A passive microwave technique for estimating rainfall and vertical structure information from space. Part I: Algorithm description. *J. Appl. Meteor.*, **33**, 3-18.

Kummerow, C., and L. Giglio, 1995: A method combining passive microwave and infrared rainfall observations. *J. Atmos. Oceanic. Technol.*, **12**, 33-45.

Kummerow, C., W. Barnes, T. Kozu, J. Shiue, and J. Simpson, 1998: The tropical rainfall measuring mission (TRMM) sensor package. *J. Atmos. Oceanic. Technol.*, **15**, 809-817.

Kurino, T., 1997, A satellite infrared technique for estimating "deep/shallow" precipitation. *Adv. Space Res.*, **19**, 511-514.

Lau, K. M., Y. Ding, J. T. Wang, R. Johnson, T. Keenan, R. Cifelli, J. Gerlach, O. Thiele, T. Rickenbach, S. C. Tsay, and P. H. Lin, 2000: A report of the field operations and early results of the South China Sea Monsoon Experiment (SCSMEX). *Bull. Amer. Meteor. Soc.*, **81**, 1261-1270.

Liu, G. R., C. C. Liu, and T. H. Kuo, 2001: Rainfall intensity estimation by ground-based dual-frequency microwave radiometers. *J. Appl. Meteor.*, **40**, 1035-1041.

Negri, A. J., R. F. Alder, and P. J. Wentzel, 1984: Rain estimation from satellites: An examination of the Griffith- Woodley technique. *J. Climate Appl. Meteor.*, **23**, 102-116.

Nystuen, J. A., and H. D. Selsor, 1997, Weather classification using passive acoustic drifters. *J. Atmos. Oceanic Technol.*, **14**, 656-666.

Nystuen, J. A., M. J. McPhaden and H. P. Freitag, 2000: Surface measurements of precipitation from an ocean mooring: The underwater acoustic log from the South China Sea. *J. Appl. Meteor.*, **39**, 2182-2197.

Prata, A. J., and R. P. Cechet, 1999: An assessment of the accuracy of land surface temperature determination from the GMS-5 VISSR. *Remote Sens. Environ.*, **67**, 1-14.

Richards, F., and F. Arkin, 1981: On the relationship between satellite-observed cloud cover and precipitation. *Mon. Wea. Rev.*, **109**, 1081-1093.

Simpson, J., C. Kummerow, W. K. Tao, and R. F. Adler, 1996: On the tropical rainfall measuring mission (TRMM). *Meteor. Atmos. Phys.*, **60**, 19-36.

Vicente, G. A., R. A. Scofield, and W. P. Menzel, 1998: The operational GOES infrared rainfall estimation technique. *Bull. Amer. Meteor. Soc.*, **79**, 1883-1898.

Wilheit, T. T., and A. T. C. Chang, 1980: An algorithm for retrieval of ocean surface and atmospheric parameters from the observations of the scanning multichannel microwave radiometer. *Radio Sci.*, **15**, 525-544.

Wilheit, T. T., A. T. C. Chang, and L. S. Chiu, 1991: Retrieval of monthly rainfall indices from microwave radiometric measurements using probability distribution functions. *J. Atmos. Oceanic. Technol.*, *8*, 118-136.

Xu, L., S. Sorooshian, X. Gao, and H. V. Gupta, 1999: A cloud-patch technique for identification and removal of no-rain clouds from satellite infrared imagery. *J. Appl. Meteor.*, **38**, 1170-1181.